crystals

MDPI

Article

Cationic-Surfactant (CTAB) Assisted Preparation of 2D Graphitic Carbon Nitride (g-C_3N_4) Sheets Advances Supercapacitive Performance

Sagar M. Mane [1], Aviraj M. Teli [2], Sonali A. Beknalkar [2], Deepak R. Patil [3,*], Jae Cheol Shin [2,*] and Jaewoong Lee [1,*]

[1] Department of Fiber System Engineering, Yeungnam University, 280 Dehak-Ro, Gyeongsan 38541, Republic of Korea
[2] Division of Electronics and Electrical Engineering, Dongguk University-Seoul, Seoul 04620, Republic of Korea
[3] School of Materials Science and Engineering, Yeungnam University, Gyeongsan 38541, Republic of Korea
* Correspondence: deepphy24@gmail.com (D.R.P.); jcshin@dgu.ac.kr (J.C.S.); jaewlee@yu.ac.kr (J.L.)

Abstract: The distinct physicochemical characteristics of metal-free graphitic carbon nitride (g-C_3N_4) are gaining interest in various fields, including energy storage and conversion. However, the electrochemical performance of this material is constrained, owing to its minimal surface area. Incorporating a surfactant is one of the ways to resolve the issue of surface area and therefore improve the electrochemical performance of g-C_3N_4. This research delves into a method aimed at improving the supercapacitive capabilities of 2D g-C_3N_4 sheets through the implementation of a cationic surfactant, cetyltrimethylammonium bromide (CTAB). Electrochemical studies reveal that the CTAB-assisted g-C_3N_4 sheets exhibit remarkable improvements in specific capacitance, cyclic stability, and comparative rate capability in relation to pristine g-C_3N_4. The specific capacitance of g-C_3N_4 with CTAB exceeds about 28%, which gives 162. 8 F g^{-1}. This value is 117.7 F g^{-1} for electrode material without CTAB at 0.5 mA cm^{-2}. This improved electrochemical performance can be credited to the heightened surface area, improved electronic conductivity, and optimized charge transfer kinetics facilitated by the CTAB surfactant. We aim to emphasize the enhancement of the overall performance of g-C_3N_4-based supercapacitors for advanced energy storage systems.

Keywords: 2D g-C_3N_4; CTAB integration; specific capacitance; current mechanism

Citation: Mane, S.M.; Teli, A.M.; Beknalkar, S.A.; Patil, D.R.; Shin, J.C.; Lee, J. Cationic-Surfactant (CTAB) Assisted Preparation of 2D Graphitic Carbon Nitride (g-C_3N_4) Sheets Advances Supercapacitive Performance. *Crystals* **2024**, *14*, 312. https://doi.org/10.3390/cryst14040312

Academic Editor: Faxing Wang

Received: 13 February 2024
Revised: 20 March 2024
Accepted: 22 March 2024
Published: 27 March 2024

1. Introduction

The rising advancements in and utilization of energy emphasize the increasing importance of exploring efficient and eco-friendly sources for energy storage and conversion. In this context, several investigators have directed their attention toward batteries and supercapacitors (SC_s), alternatively called ultracapacitors or electrochemical capacitors, as primary devices for storing energy [1–3]. These devices are primarily useful for revitalizing contemporary technological applications, including smart electronics, electronic/hybrid vehicles, and wearable and stretchable devices [4]. In recent decades, the compact designs of these devices have been found to be applicable as an integrated power source for the automatization of vehicle windows, foldable displays for computers and mobiles, field-effect transistors, health tracking devices, etc. [5]. The appealing characteristics of supercapacitors include energy densities that surpass conventional capacitors, extended cycle life, and enhanced power densities compared to batteries [6]. These qualities and their safe operation make them highly prominent across various applications [7–9]. In the twenty-first century, lightweight, portable, miniaturized, and flexible gadgets have attracted a lot of interest among the above-mentioned applications. Designing electrode materials with excellent electrical ability, eminent mechanical durability, and the longest possible span of continuous performance to fulfill the requirements of such applications

is a substantial challenge at present [10–13]. Hence, researchers globally have focused on conducting thorough investigations into the development of the materials needed to meet the current demands. Commonly utilized materials for lightweight and flexible supercapacitors include conducting polymers, metal oxides/hydroxides, carbon derivatives, and various composites of these species [12]. In addition to these, there is a predominant focus on investigating semiconductors or 2D materials like MoS_2, WS_2, V_2O_5, g-C_3N_4, SnO_2, WO_3, and WS_2, which are predominantly under investigation to develop electrodes for energy storage devices [8,14,15].

Due to its impressive electrical configuration, outstanding structural stability, and environmentally friendly properties, graphitic carbon nitride (g-C_3N_4), from the affordable redox-active semiconductor family, is considered a viable option for electrode material. The two-dimensional (2D) graphite-like structure of g-C_3N_4 further enhances its potential applications in flexible electrode technology [16,17]. This material represents a stable structural variant within carbon nitride, featuring a hexagonal arrangement formed by σ bonds. Additionally, it exhibits an extensively dispersed π-conjugated system: a result of carbon and nitrogen's sp^2 hybridization [18]. The van der Waals interactions resulting from π-orbitals between individual layers contribute to the outstanding thermal and chemical stability of g-C_3N_4. Combining this with its advantageous electronic structure, with a bandgap (Eg) of about 2.7 eV, g-C_3N_4 becomes an outstanding material for a wide range of applicability. Its utilization spans catalysis, pollutant degradation, bioimaging, light-emitting diodes, photocatalytic applications, and various other applications [19–23]. Additionally, this material's layered characteristics contribute to substantial surface-to-volume ratios, further amplifying, significantly, the efficient utilization of active sites. Consequently, this results in improved electrochemical performance, leading to a reduction in the distances for both electronic and ionic transfers [24]. This renders it notable as an electrode material in energy storage devices. However, when viewed as a possible electrode, unmodified g-C_3N_4 exhibits poor long-term stability and restricted electrochemical performance. Additionally, the Van der Waals force is responsible for g-C_3N_4 nanosheets' tendency to agglomerate, which results in decreased specific power and energy density [5].

Hence, it is imperative to devise and explore additional strategies aimed at enhancing the electrochemical performance of this material. In this context, a method that entails the creation of hybrid or composite electrodes utilizing this material was employed by a few researchers. This was achieved by integrating it into a conductive species or incorporating semiconductor materials. This enhances surface activity, thereby contributing to improved performance [25]. Even though g-C_3N_4 exhibits numerous advantages as an electrode material in energy storage applications, there has been limited research focused on enhancing its electrochemical properties. Several protocols have been devised to improve the capacitive behavior of materials. This includes proton flow within nanomaterials, electron tunneling or hopping, and the spinning of electrons between the current collector (conducting substrate) and active electrode material. In this regard, the works of Y. Gao et al. [26] and D. Ilager et al. [27] have investigated the introduction of CTAB as a cationic surfactant, which serves as a strategic tool in overcoming the above-mentioned challenges associated with g-C_3N_4. CTAB offers a versatile platform for the controlled synthesis of two-dimensional g-C_3N_4 sheets by stimulating the surface pores. Furthermore, it impedes the clumping together of particles and increases the number of active sites, which is favorable for electrochemical energy storage purposes.

Therefore, through this research work, we aimed to thoroughly analyze the electrochemical performance of graphitic carbon nitride (g-C_3N_4) prepared with and without the incorporation of the cationic surfactant, CTAB. The ensuing discussion will unveil the noteworthy influence of CTAB interaction in customized g-C_3N_4 sheets on supercapacitive performance. This will provide insights into heightened capacity, a detailed understanding of the charge–storage mechanism, and prolonged cycling stability. We observed that the specific capacitance of g-C_3N_4 with CTAB increases by about 28% when compared with g-C_3N_4 prepared without CTAB. This electrode also dominates in terms of cycling stability

by retaining 75.1% of capacitance after 5000 charge–discharge cycles, which was 69.8% for electrode material without CTAB.

2. Experimental Section

2.1. Chemicals and Materials

The analytical grade precursors of melamine and cetyltrimethylammonium bromide (CTAB) required to prepare g-C_3N_4 and g-C_3N_4(CTAB) were bought from Sigma-Aldrich, St. Louis, MO, USA.

2.2. Preparation of 2D Graphitic Carbon Nitride (g-C_3N_4)

Pure g-C_3N_4 and surfactant-assisted g-C_3N_4 were synthesized by subjecting melamine powder to thermal condensation. To produce pure g-C_3N_4, the following procedure was employed: 5 g of melamine powder were directly placed into an alumina crucible, sealed with a cap. Additionally, the crucible was securely wrapped in aluminum foil and positioned at the center of the programmable tube furnace. The melamine-powder-containing crucible was subjected to heating at a rate of 4 °C per minute, reaching a temperature of 550 °C, which was then maintained for 4 h. It was subsequently cooled to room temperature, and the resulting yellow-colored product was gathered. In another approach, a similar process was repeated to get the g-C_3N_4: in this case 5%, i.e., 0.25 g of cationic surfactant CTAB was added with the melamine. In this instance, the final product achieved had changed to a pale gray color from yellow.

2.3. Characterization of g-C_3N_4

For confirmation of the crystallization of pure g-C_3N_4, along with the inclusion of CTAB, an X-ray diffractometry (XRD) technique was employed to analyze the structure and phase of the products generated after thermal condensation. DIATOMS-Panalytical equipment (Malvern, London, UK) was used to gather diffraction patterns among 2θ = 10 to 70° with Cu Kα radiation (λ = 1.5418 Å). Surface topology was examined using Field Emission Scanning Electron Microscopy (FE-SEM; S-4800, Hitachi, Ibaraki, Japan), and the elements composing the samples were determined using Energy-Dispersive X-ray Spectroscopy (EDS). For in-depth analysis of morphology, Field Emission Transmission Electron Microscopy (FE−TEM; Tecnai G2 F20 S−TWIN, Hillsboro, OR, USA) was used. The surface chemistry, carbon and nitrogen composition, and chemical bonding of C and N in g-C_3N_4 were analyzed by X-ray Photoelectron Spectroscopy (XPS; Versaprobe II, ULVAC-PHI Inc., Chigasaki, Kanagawa, Japan). Nitrogen adsorption–desorption isotherm was recorded to evaluate the surface area (BET method) and pore diameter (BJH method) of both samples (Micromeritics; 3-flex analyzer, Norcross, GA, USA).

2.4. Fabrication of Electrode and Electrochemical Measurements

The active material obtained through thermal condensation of melamine and CTAB-integrated melamine was blended with carbon black polyvinylidene fluoride (PVDF) in a ratio of 80:10:10 using N-methyl-2-pyrrolidinone. The blended slurries were subsequently applied onto a 1 cm^2 area of a piece of nickel foam and dried up using a heating oven at 90 °C for 12 h. Before applying slurries of active material blended with carbon black and PVDF, the Ni foam underwent ultrasonic treatment using acetone, ethanol, and water, individually. To assess the mass loading, we measured the weight of the Ni foam both before applying slurries and after undergoing the drying treatment. From this, the confirmed mass loading was 1.2 $mg.cm^{-2}$ for the electrode of pure g-C_3N_4 while it was 1.3 $mg.cm^{-2}$ for CTAB-integrated g-C_3N_4. Electrochemical assessments were conducted, employing an electrochemical workstation ZIVE SP5 (WonaTech; Seocho-gu, Seoul, Republic of Korea). Three electrodes were immersed in a 2 mol/L KOH and different tests, such as cyclic voltammetry (CV), charge–discharge (GCD) profile at constant current, and electrochemical impedance spectroscopy (EIS), on both electrodes were carried out. In this assembly of three electrodes, the working electrodes, counter electrode, and reference electrode utilized were

based on Ni foam coated with g-C_3N_4, a graphite plate, and standard calomel electrode (SCE), respectively. The optimization of g-C_3N_4 electrode performance, both with and without CTAB, involved utilizing the mass of active material (m) deposited onto a 1 cm^2 area (A) of Ni foam, along with the voltage range (ΔV) and discharge time (t_d) determined from the discharge profiles of each electrode. To achieve this objective, the following expressions were employed [28]:

$$C_s = \frac{I \times t_d}{m \times \Delta V} \quad (1)$$

$$C_A = \frac{I \times t_d}{A \times \Delta V} \quad (2)$$

3. Results and Discussion

Figure 1a represents the X-ray diffraction patterns for graphitic carbon nitride (g-C_3N_4) prepared through the thermal condensation process. The black color diffraction pattern was assigned to g-C_3N_4 without CTAB, and for CTAB-integrated g-C_3N_4 it was illustrated by the red color. Diffraction patterns of both samples were indexed as per JCPDF card number 087-1526 and indicate hexagonal crystallinity with space group $P\bar{6}m2$. The crystal planes noted at 2θ angles of 12.84° (001) and 27.68° (002), through thermal condensation of melamine without CTAB, effectively confirm the formation of graphitic carbon nitride [29]. These planes reflect the in-plane ordering of units of the tri-s-triazine and layer-to-layer distance, respectively [30]. Although the recurrence of this diffraction pattern was noted during the thermal condensation of melamine integrated with CTAB, therein lies a very small difference. This difference lies in the 2θ positions of those crystal planes. Here, the incorporation of a minimal quantity of cationic surfactant caused a displacement of the characteristic peaks of g-C_3N_4 to a lower 2θ angle. The negative shift, i.e., shifting towards a lower 2θ angle, can be visualized through Figure 1b for the (002) crystal plane. The negative shift in the XRD diffraction peak is assigned to lattice expansion or an increase in the interlayer distance of g-C_3N_4. Furthermore, alterations in the Full Width at Half Maximum (FWHM) serve as reliable indicators to validate the influence of CTAB on crystallinity [29,31].

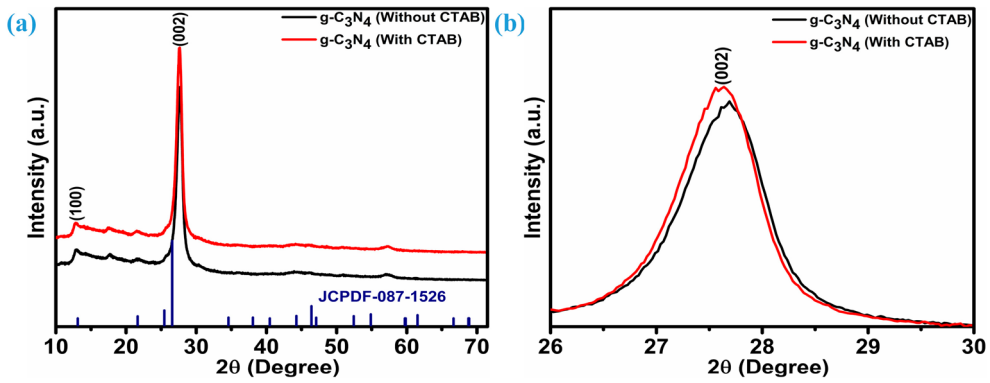

Figure 1. X-ray diffraction analysis, (**a**) diffraction patterns of g-C_3N_4 without and with CTAB, (**b**) enlarged view of (002) plane.

X-ray photoelectron spectroscopy (XPS) assessment was undertaken to learn more about the chemical composition of nitrogen and carbon within the fabricated g-C_3N_4 without and with CTAB. Survey spectra illustrated in Figure 2a for both samples of the g-C_3N_4 (black color line without CTAB, red color line with CTAB) revealed the detection of only three elements: carbon (C), nitrogen (N), and oxygen (O). Carbon and nitrogen are the prime elements of g-C_3N_4 samples, while the oxygen peak comes from the handling of the samples. Figure 2b,c display a high-resolution C 1s spectrum of the g-C_3N_4 sample without and with CTAB, respectively. These C 1s spectrums can be accurately represented by fitting three distinctive peaks integrated within them using Gaussian–Lorentzian profiles.

These three peaks are associated with the distinct carbon species in the graphitic carbon nitride [32]. Interestingly, for both samples of g-C_3N_4, i.e., without CTAB, when cationic CTAB propagated through the 2D sheets the binding energy position of these peaks carbon species remained unchanged. In both cases, these peaks were located at 284.6, 288.0, and 288.9 eV, respectively. One of the carbon species integrated within the C 1s spectrum can be identified as pure sp^2 carbon (C–C) or a C=C bond, reminiscent of the free/impure carbon species. The corresponding peak for this species is positioned at a lower binding energy, specifically at 284.6 eV [8,33,34]. A sharp central peak identifies the tri-s-triazine unit, as does the pyridine-like structure inside the aromatic ring system. In particular, this peak is associated with sp^2 carbon–nitrogen (N–C–N) bonds. The binding energy position of this peak is 288.0 eV. The peak with higher binding energy, at 288.9 eV, is designated for covalent bonding in the C–N network of tertiary (3°) carbon with the three nitrogen atoms. This peak is an indication of a graphitic-like nitrogen structure [35]. Similar to the C 1s spectrum, the three distinctive peaks are incorporated within the high-resolution nitrogen (N 1s) spectrum and this scenario is for both samples of g-C_3N_4, as illustrated in Figure 2d,e for samples without and with CTAB, respectively. As illustrated, one tall peak and two other broad peaks inside the N 1s spectrum reflect that nitrogen species were located at binding energies of 398.5, 399.4, and 401.0 eV, respectively. The prime intensive peak at the lowest binding energy, 398.5 eV, identifies the sp^2-bonded nitrogen with graphitic carbon (–C=NH) present in the triazine rings. The broad peak next to this peak is positioned at a higher binding energy, i.e., 399.4 eV is associated with nitrogen atoms adopting a sp^2-configuration and being bonded to two carbon atoms [30,36]. The third peak is located at a higher binding energy of 401.0 eV, designated for nitrogen atoms trigonally bonded to all sp^2 carbons [37].

Field Emission Scanning Electron Microscopy (FE-SEM) was utilized to examine the microscopic characteristics of the 2D g-C_3N_4 without and with CTAB. Figure 3a–f yield comparable morphological views for g-C_3N_4 samples without and with CTAB at different magnifications (500 nm, 2 μm, and 5 μm). Several smaller particles contribute to generating irregularly shaped big lumps in both samples with or without CTAB (Figure 3a,d). Maximum irregular lump formation was observed in samples lacking CTAB, which can be noticed through lower magnification images, as in Figures 3b and 3c. Nevertheless, the introduction of CTAB results in the formation of a stacked arrangement of multiple wrinkled layers with small particles, thus, the g-C_3N_4 structure takes on a sheet-like appearance. The formation of stacked layers of sheets can be easily noticed in Figure 3e,f for the CTAB integrated sample. Moreover, these stacked layers were spongy, as seen in Figure 3f, which makes intercalation/deintercaltion electrolytic ions with easy way. The Energy Dispersive Spectroscopy (EDS) examination identifies signals corresponding to C and N only as illustrated in Figure 4a,b, respectively. This affirmed the presence of composed elements in both samples and revealed impurity-free development of g-C_3N_4, irrespective of whether CTAB was included or not. The table insight of the EDS spectrum gives weight (%) and atomic percentage of the carbon and nitrogen species. The formation of g-C_3N_4 takes place with a ratio of 1:1.32 between carbon and nitrogen for the sample without CTAB, while it tends to be 1:1.39 with the inclusion of CTAB.

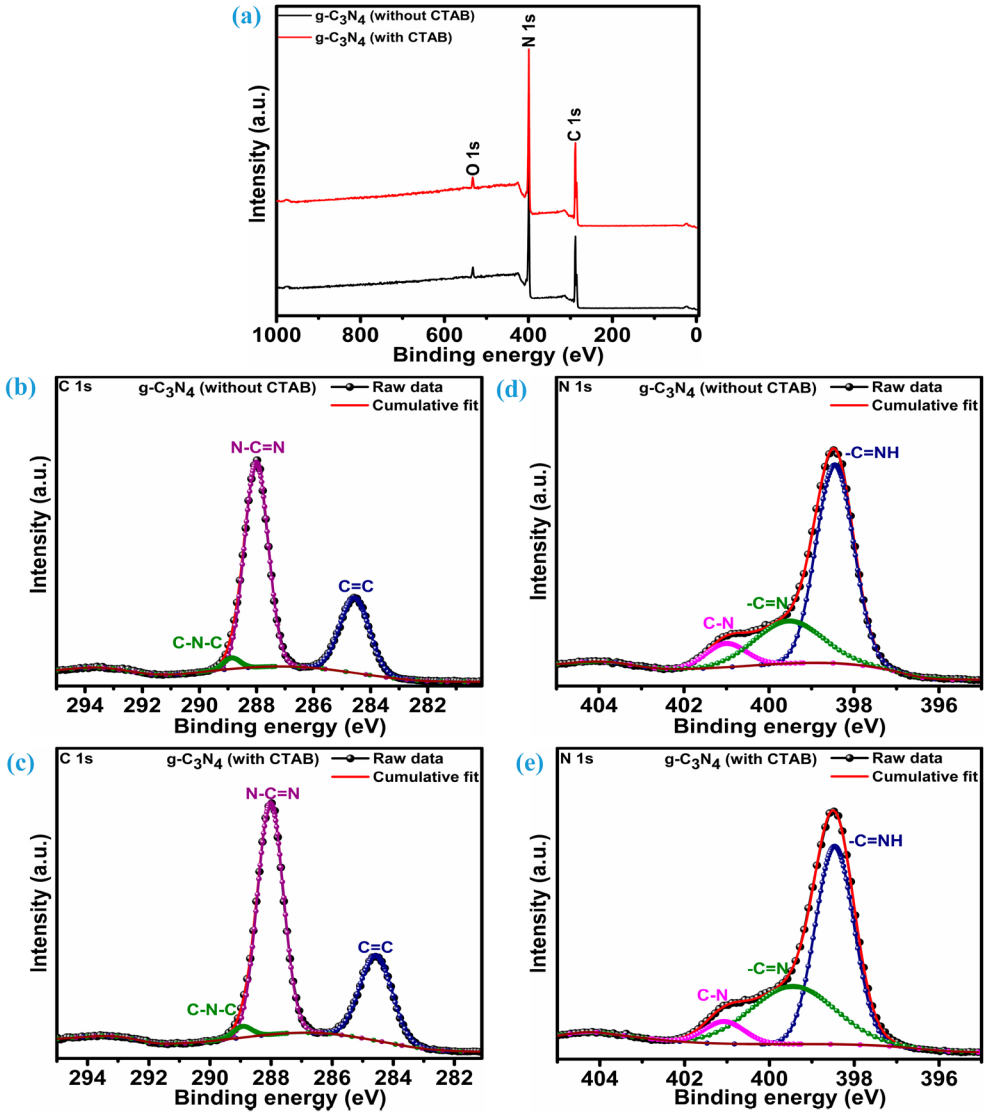

Figure 2. XPS analysis, (**a**) survey spectrum of g-C_3N_4 without and with CTAB, (**b**) C 1s spectrum of g-C_3N_4 without CTAB, (**c**) C 1s spectrum of g-C_3N_4 with CTAB, (**d**) N 1s spectrum of g-C_3N_4 without CTAB, and (**e**) N 1s spectrum of g-C_3N_4 integrated with CTAB.

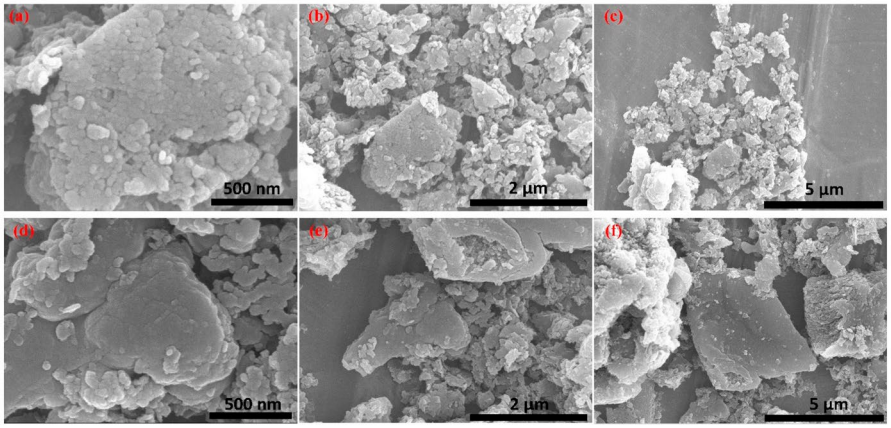

Figure 3. FE-SEM analysis, (**a**–**c**) different magnification FE-SEM images of g-C_3N_4 without CTAB, and (**d**–**f**) different magnification FE-SEM images of g-C_3N_4 with CTAB.

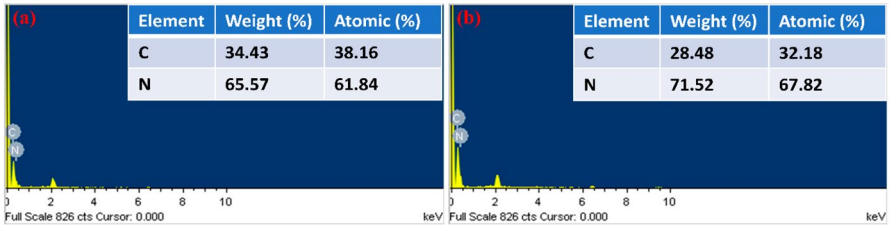

Figure 4. Elemental analysis using EDS, (**a**) EDS spectrum of g-C_3N_4 without CTAB, and (**b**) EDS of g-C_3N_4 with CTAB.

TEM was further used to highlight the in-depth morphology of the g-C_3N_4 samples without and with CTAB. TEM, HR-TEM images, and SAED patterns of the g-C_3N_4 samples without CTAB are represented in Figure 5a–d while Figure 5e–h illustrates the g-C_3N_4 integrated with CTAB. TEM and HR-TEM confirm wrinkled 2D sheet-like features for both samples, however, the sheets of the g-C_3N_4 sample without CTAB are slightly aggregated and thicker than the sample with CTAB integration. SAED confirms that both samples are amorphous.

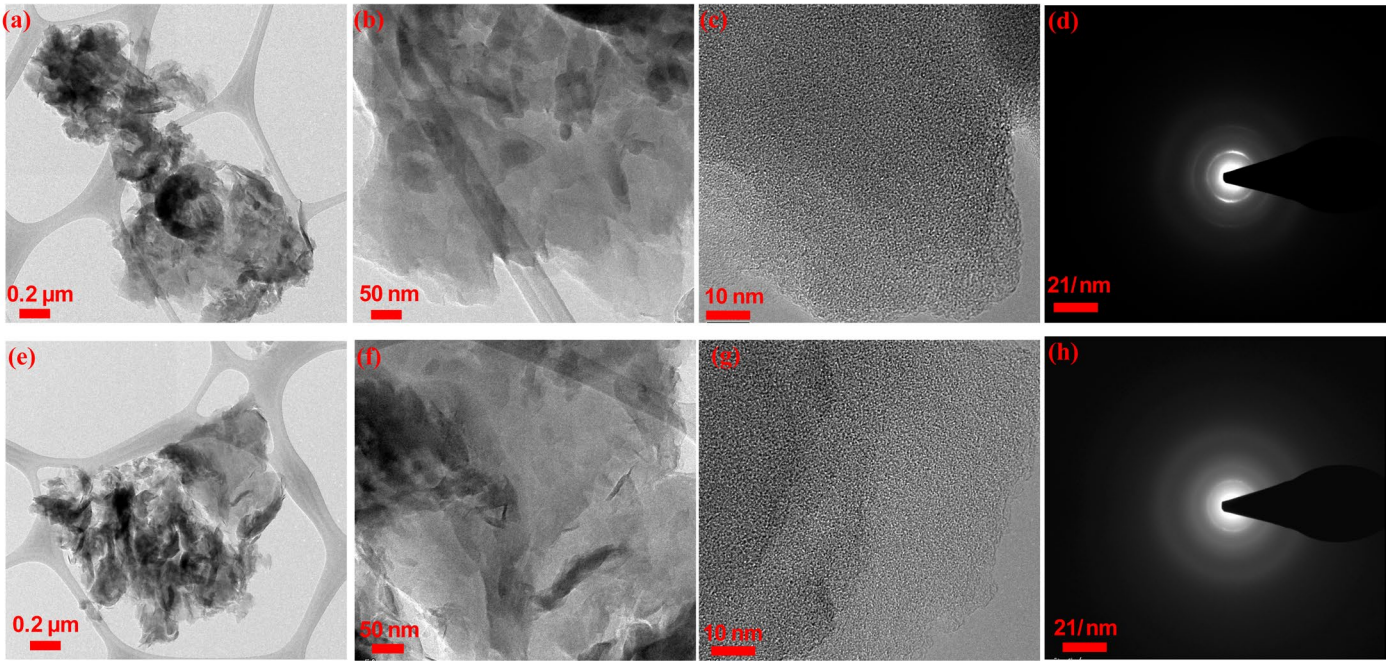

Figure 5. TEM analysis, (**a**,**b**) TEM images of the g-C_3N_4 without CTAB, (**c**) HR-TEM image of g-C_3N_4 without CTAB, (**d**) SAED pattern of g-C_3N_4 without CTAB, (**e**,**f**) TEM images of g-C_3N_4 with CTAB, (**g**) HR-TEM image of g-C_3N_4 with CTAB, and (**h**) SAED pattern of g-C_3N_4 without CTAB.

In this work, the g-C_3N_4 samples were prepared using the thermal treatment of melamine which was conducted at 550 °C. This temperature is higher than that of the decomposition temperature of the CTAB, which is 300 °C. Through the literature, it was found that even when the decomposition of the CTAB takes place it is beneficial due to the creation of a large number of uniform pores and enhancing of the surface area. Because of the gases released (O_2, CO_2, H_2O) during the decomposition of CTAB, pores are created that are in equal dimensions to those of surfactant [38]. Therefore, to analyze the effect of CTAB integration on the surface area and pore size distribution of g-C_3N_4, nitrogen adsorption-desorption isotherms were measured. N_2 isotherms for g-C_3N_4 without CTAB and with CTAB are represented in Figure 6a,b, respectively, and the pore size distribution is represented in the figure inset. Isotherms of both samples display classical type IV patterns with proper H3 hysteresis curves. CTAB-integrated g-C_3N_4 was found to be richer

in the surface area, exhibiting 17.19 m^2/g, whereas that of the g-C_3N_4 sample without CTAB exhibited a surface area of 12.82 m^2/g when measured using the Brunauer–Emmett–Teller (BET) method. Furthermore, the pore size distribution inset, derived based on the Barret–Joyner–Halender (BJH) method, illustrates a broad range of pore sizes. The curve reflects the average pore width of 25 nm for CTAB-integrated g-C_3N_4 and 30 nm for that without CTAB. Increased surface through CTAB integration is useful for boosting the overall electrochemical performance of the g-C_3N_4.

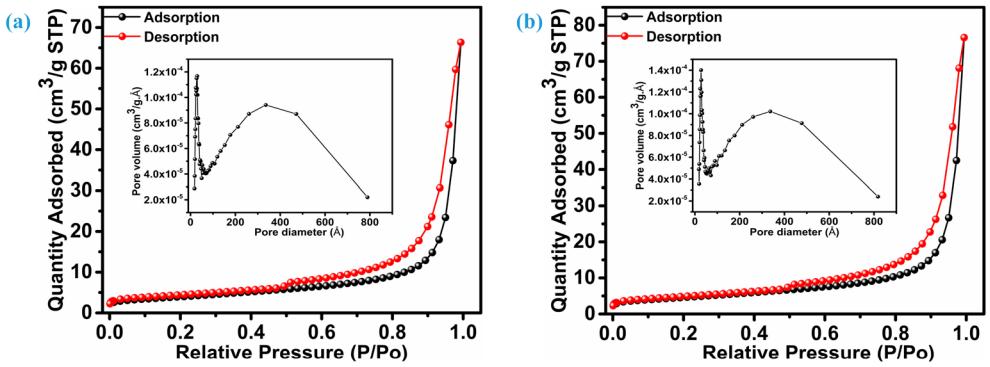

Figure 6. Surface area analysis, (**a**) nitrogen adsorption-desorption isotherm of g-C_3N_4 without CTAB, and (**b**) nitrogen adsorption-desorption isotherm of g-C_3N_4 with CTAB. Figures inset are pore volume vs. pore diameter curves.

This section delineates the functional attributes of g-C_3N_4 and examines the influence of incorporating a cationic surfactant on these properties. In this regard, the electrochemical characteristics (CV, GCD, and EIS) were investigated with a three-electrode setup using active electrodes on Ni foam prepared using g-C_3N_4 without and with CTAB. Figure 7a illustrates a comparative analysis of the electrochemical performance between pristine g-C_3N_4 and g-C_3N_4 integrated with CTAB. The testing was conducted in a 2 mol/L aqueous KOH solution, and the recorded cyclic voltammetry (CV) curves were obtained at a scan rate of 10 mV s^{-1} and voltage window of −0.1 to 0.6 V. The reversible Faradaic redox features confirm the two distinct asymmetrical redox peaks and suggest that the electrochemical activity of g-C_3N_4 is associated with pseudocapacitivity. Both electrodes have the same features, however, conversely, the electrode fabricated through integrating CTAB is accompanied by an enhanced current response/high area under the CV curve. Reversible redox peaks in the CV profile are an indication of interaction between electrodes and electrolytes; this process of interaction can be articulated as follows [8].

$$g - C_3N_4 + 2OH^- \leftrightarrow g - C_3N_4(OH)_2 + 2e^- \quad (3)$$

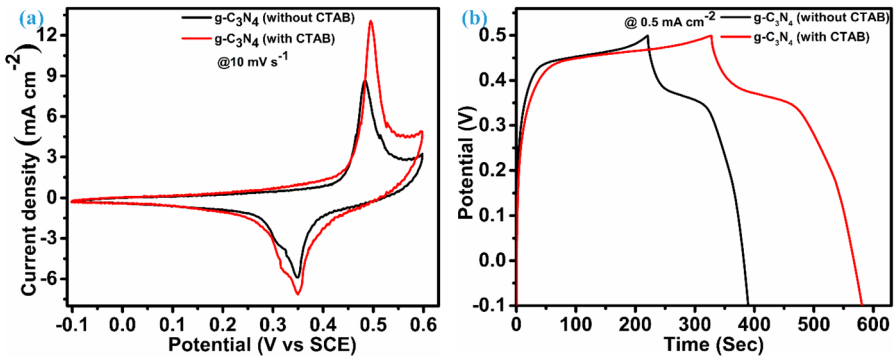

Figure 7. Comparative electrochemical analysis of g-C_3N_4 without and with CTAB, (**a**) CV at 10 mV s^{-1}, and (**b**) charge-discharge curve at 0.5 mA cm^{-2}.

Figure 7b illustrates the comparative Galvanostatic Charge–Discharge (GCD) curves at 0.5 mA cm^{-2}. The GCD curves of both g-C_3N_4 electrodes exhibited symmetric curves portraying exceptional charge–discharge characteristics, with impressive coulombic efficiency and minimal polarization. Moreover, the alignment of the GCD curve with CV analysis is notable, especially in the context of the CTAB-integrated g-C_3N_4 electrode. GCD gives a crucial parameter required for assessing the capacitive performance of the electrode material, which is nothing but discharging duration. Herein, the CTAB-integrated electrode outperforms the electrode material without CTAB. At the same current density of 0.5 mA cm^{-2}, the electrode of g-C_3N_4 with CTAB renders 254 s of discharging time and that of the electrode without CTAB can give 169 s. This enables a specific (areal) capacitance of 162.8 F g^{-1} (211.7 mF cm^{-2}) for the CTAB-integrated electrode, which is 117.3 F g^{-1} (140.8 mF cm^{-2}) in the case of g-C_3N_4 without CTAB.

To shed light on the charge–transfer dynamics, diffusion coefficient, and formal oxidation and reduction capabilities of the active material, we further conducted a scan rate dependence analysis of the cyclic voltammetry (CV) for each electrode. Figure 8a,b illustrate the scan rate dependence CV profile for g-C_3N_4 without CTAB and upon integrating CTAB, respectively. The consistency of the CV curves in the case of both electrodes persists as the scan rate varies from a lower limit of 5 to a higher 100 mV s^{-1}. CV profiles of both electrodes reflect analogous patterns, with no notable variations even when subjected to elevated scanning speeds. This proves that g-C_3N_4-based electrodes have good reversible charge–transfer dynamics and rate capability [39,40]. As anticipated, a dual set of Faradaic redox peaks is set to appear when the reversible redox scanning takes place from a low scan rate to a high scan rate in both electrodes. This unveils that g-C_3N_4 electrodes are equipped with battery-like characteristics owing to intercalation and de-intercalation of electrons/ions within interlayers of the nanosheets [41]. Slight displacement of anodic and cathodic peaks around higher and lower potentials occur, respectively, when the scan rate is changed from low to high, which elucidates an inadequate diffusion rate of ions. This phenomenon hinders the attainment of oxidation–reduction reactions, commonly referred to as electrode polarization [42]. The peak current (reduction–oxidation peaks) of CV at each scan rate was estimated and plotted with the square root of the scan rate and fitted linearly as illustrated in Figure 8c. The determination of the slope from the linear fitting of this graph was employed to evaluate the diffusion of K^+ ions in both electrodes, in accordance with the Randle–Sevcík equation [43].

$$i_p = 0.4463 \times n \times F \times C \times A \times \sqrt{\frac{nFvD}{RT}} \quad (4)$$

where variables are n (number of electrons involved in the reaction), F (Faraday constant), A (active electrode area), C (concentration of the electrolyte), D (reactant diffusion factor), R (gas constant), T (temperature), v (scan rate of CV measurement). Considering the constant parameters and variables from voltammetric experiments, Equation (4) can be rewritten as:

$$\frac{i_p}{v^{1/2}} = 2.69 \times 10^5 \times A \times C \times D^{\frac{1}{2}} \times n^{\frac{1}{2}} \quad (5)$$

Therefore, by analyzing the slope from Figure 8c, we estimated the diffusion coefficients for the g-C_3N_4 without and with CTAB. In contrast to the g-C_3N_4 without CTAB, the diffusion coefficient for the CTAB-integrated electrode material exhibited a noteworthy increase. The values of the diffusion parameter for g-C_3N_4 without CTAB remain 2.61×10^{-3} cm^3 s^{-1} and 2.14×10^{-3} cm^3 s^{-1} during the reversible reduction and oxidation processes, respectively. These values shift to 3.33×10^{-3} cm^3 s^{-1} and 2.35×10^{-3} cm^3 s^{-1} for g-C_3N_4 with CTAB inclusion. CTAB integration enhances the diffusion coefficient, which may be attributed to its spongy stacked-layered structure of 2D sheets (as noticed in FE-SEM). This structure provides enormous diffusion sites, boosting the diffusion process capability.

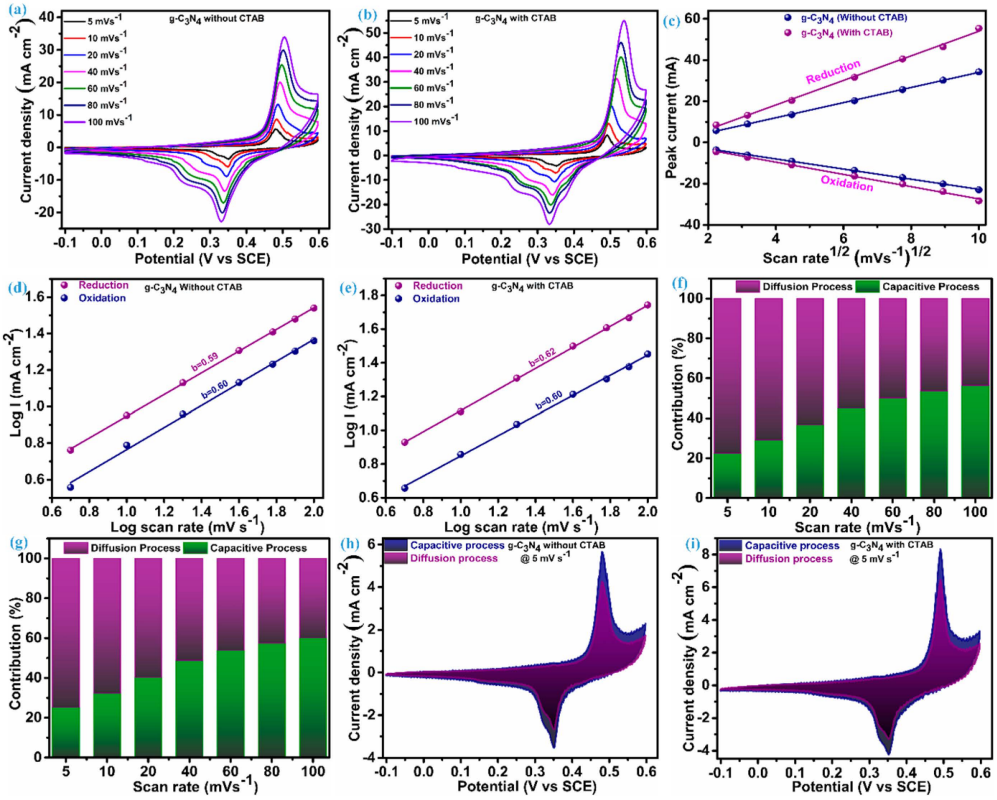

Figure 8. Charge storage mechanism study of g-C_3N_4 electrodes without and with CTAB, (**a**) CV at different scans of g-C_3N_4 electrode without CTAB, (**b**) CV at different scans of g-C_3N_4 electrode with CTAB, (**c**) redox peak current vs. square root of scan rate for both electrodes, (**d**) log(i) vs. log(v) plot of g-C_3N_4 electrode without CTAB, (**e**) log(i) vs. log(v) plot of g-C_3N_4 electrode with CTAB, (**f**) charge storage quantification of g-C_3N_4 electrode without CTAB, (**g**) charge storage quantification of g-C_3N_4 electrode with CTAB, (**h**) CV curve at 5 mV s^{-1} reflecting charge storage quantification of g-C_3N_4 electrode without CTAB, and (**i**) CV curve at 5 mV s^{-1} reflecting charge storage quantification of g-C_3N_4 electrode with CTAB.

The electrodes of supercapacitors belong to a distinctive category, utilizing both electrostatic and electrochemical phenomena for charge storage. The charge storage functioning of supercapacitor electrodes can be retrieved in terms of two different approaches: capacitive and diffusion-controlled. To comprehend the charge storage mechanism within g-C_3N_4 electrodes without and with the inclusion of CTAB, we analyzed the correlation between the scan rate (v) and redox peak current (i_p) derived from cyclic voltammograms and measured at different scan rates. Therefore, based on the power law, the linear curves of log(i) vs. log(v) were utilized to explore the kinetics of the charge storage mechanism within the manufactured electrodes. These log(i) vs. log(v) curves are illustrated in Figure 8d,e for gC_3N_4 electrodes without CTAB and with CTAB, respectively. In general, this power law is commonly known as b-value assessment and can be expressed as follows [44]:

$$i_p = i_{surface} + i_{diffusion} = ab^v \quad (6)$$

The "b-value" in this equation is nothing but a slope of the linear fitting of those curves represented in Figure 8d,e. This value serves as a determinant for either surface-controlled or diffusion-controlled charge storage mechanisms in the electrode material. Typically, a capacitive-controlled charge storage kinetic scenario is characterized by a value of b = 1, while a diffusive-controlled scenario is associated with a value of b = 0.5. As represented in Figure 8d,e, the b-values for the g-C_3N_4 electrodes without CTAB and with integrated CTAB are 0.60 and 0.62, respectively. These values manifest a biased nature in the K^+ charge storage kinetics of our electrodes, with the diffusion-controlled

(Faradaic) mechanism surpassing the surface-controlled (non-Faradaic) mechanism. To assess the diffusion-controlled and surface-controlled current in our electrodes, an analysis that depends on scan rate (v) and utilizes the current response (i) at a constant voltage is conducted using the following equation [45]:

$$i(V) = k_1\nu + k_2\nu^{1/2} \quad (7)$$

The k_1 and k_2 represent the charge storage kinetics originating from surface-controlled and diffusion-controlled scenarios, respectively. Figure 8f,g illustrates the capacitive and diffusion contribution across different scan rates of the g-C_3N_4 electrode without and with CTAB, respectively. As seen through these figures, the contribution of the diffusion mechanism is superior at lower scan rates and surface-controlled capacitance shows a progressive rise as scan rates increase. This increase indicates an intensified dependence on the scanning rate of the surface-controlled mechanism [46]. Quantification rectifies surface-controlled mechanism progress from 22.5% at 5 mV s^{-1} to 56.5% at 100 mV s^{-1} for g-C_3N_4 prepared without CTAB. Additionally, with the incorporation of CTAB, the g-C_3N_4 electrode exhibits a gradual shift toward the surface-controlled mechanism. Specifically, at a scan rate of 5 mV s^{-1}, this mechanism contributes 25.3% to the current, and as the scan rate increases to 100 mV s^{-1}, its contribution rises to 60.2%. The CV curves depicted in Figure 8h,i, obtained at a scan rate of 5 mV s^{-1}, illustrate the electrochemical behavior of electrodes of g-C_3N_4 without and with CTAB, respectively. These curves signify the integrated area, encompassing the current contributions from both diffusion-controlled and surface-controlled processes.

The comparative analysis of both electrodes validates that the incorporation of the cationic surfactant enhances the electrochemical performance of graphitic carbon nitride. To delve deeper into the effect of alteration in current densities on the specific (areal) capacitance, rate capability Galvanostatic charge–discharge (GCD) curves were recorded within the range of 0.5 to 5 mA cm^{-2}. Figure 9a,b illustrate the GCD profile of g-C_3N_4 without CTAB and with CTAB, respectively. The GCD curves here are quite symmetric even at increasing current density. The prominent characteristics of the charge–discharge profile signify a pseudocapacitive nature, arising from the reversible electrochemical reactions occurring at the interface (electrode–electrolyte) [41]. The deductions made from the GCD profile align with the redox characteristics observed in the cyclic voltammetry (CV) of each electrode. Specific capacitance estimated as per equations (1) and (2) are illustrated in Figure 9c, wherein the CTAB-integrated electrode clearly surpasses the non-CTAB-integrated electrode at each current density. The comparative perspective of the g-C3N4-based electrodes was summarized in Table S2. The rate capability performance of the g-C_3N_4 without the CTAB electrode slightly exceeds that of g-C_3N_4 with the CTAB electrode when the current density is increased by 10 times. This electrode exhibits 54.5% capacitance retention and the CTAB-integrated electrode can retain 51.6% of capacitance at initial current density, which is as illustrated in Figure 9d.

Figure 10a,b illustrate the enduring cycling stability of the g-C_3N_4 electrodes without CTAB and with CTAB, respectively. After undergoing 5000 charge/discharge cycles at 10 mA cm^{-2}, the CTAB-integrated electrode retained a higher capacitance of 74.9% of its initial capacity, maintaining a high coulombic efficiency of 108%. On the other hand, the g-C_3N_4 electrode without CTAB can retain 70.8% with a coulombic efficiency of 106%. The specific capacitance was further measured by using GCD before and after stability at 3 mA cm^{-2}, as shown in Figure 10c,d for electrodes without and with CTAB, respectively. This analysis indicates that an electrode without CTAB at 3 mA cm^{-2} gives a specific capacitance of 57.2 F g^{-1} after stability, which is 80.6 F g^{-1} before stability. In the case of the electrode integrated with CTAB, the specific capacitance is 74.4 F g^{-1} after stability and 102.3 F g^{-1} before stability. Stacked sheets were still noticed for the CTAB-integrated g-C_3N_4 while the sheet-like structure is somewhat disturbed in the case of the g-C_3N_4 without CTAB. This was confirmed through the measurement of FE-SEM after stability analysis as represented in Figure S1a–f in the Supplementary Materials for g-C_3N_4 without

and with CTAB, respectively. The optimum performance sample (with CTAB g-C_3N_4) was further analyzed using XPS to confirm the chemical composition after a prolonged stability test. Figure S2a represents the survey XPS spectrum of the Ni-foam-loaded CTAB-integrated g-C_3N_4 after stability, which confirms the presence of carbon (C), nitrogen (N), oxygen (O), nickel (Ni), and potassium (K). The presence of Ni is attributed to the current collector (Ni foam) used to deposit the g-C_3N_4, while the K peak is due to prolonged insertion–desertion of the KOH electrolyte in the g-C_3N_4. Even after the cyclic stability, the existence of carbon and nitrogen species was confirmed through the deconvolution of the C 1s and N 1s spectrum, which is as before stability. The only change was noticed in the C 1s spectrum which shows an additional peak, indicating the influence of oxygen atoms. This oxygen may result from the longer cycling test. Deconvoluted C 1s and N 1s spectrums are represented in Figure S2b,c, respectively. The electrochemical impedance spectroscopy (EIS) spectra, presented in Figure 10e–h, depict the characteristics of the g-C_3N_4 electrode without a CTAB and with CTAB, respectively, both before and after the stability test. EIS spectra of both electrodes reflect negligible changes in all regions. The EIS spectrums were fitted using ZMAN software version 2.3.2, and an equivalent circuit of fitting is illustrated in Figure 10i. This includes the intersection at the *x*-axis, mid-frequency semicircular region, and low-frequency straight line region connected in series. The intersection region gives Equivalent Series Resistance (ESR) and it is nearly constant even after stability, indicating minimal ohmic loss. The confirmation of diffusion resistance is also supported by the slope parallel to the imaginary axis in the low-frequency region called the Warburg diffusion element. Values of each element after fitting are illustrated in Table S1.

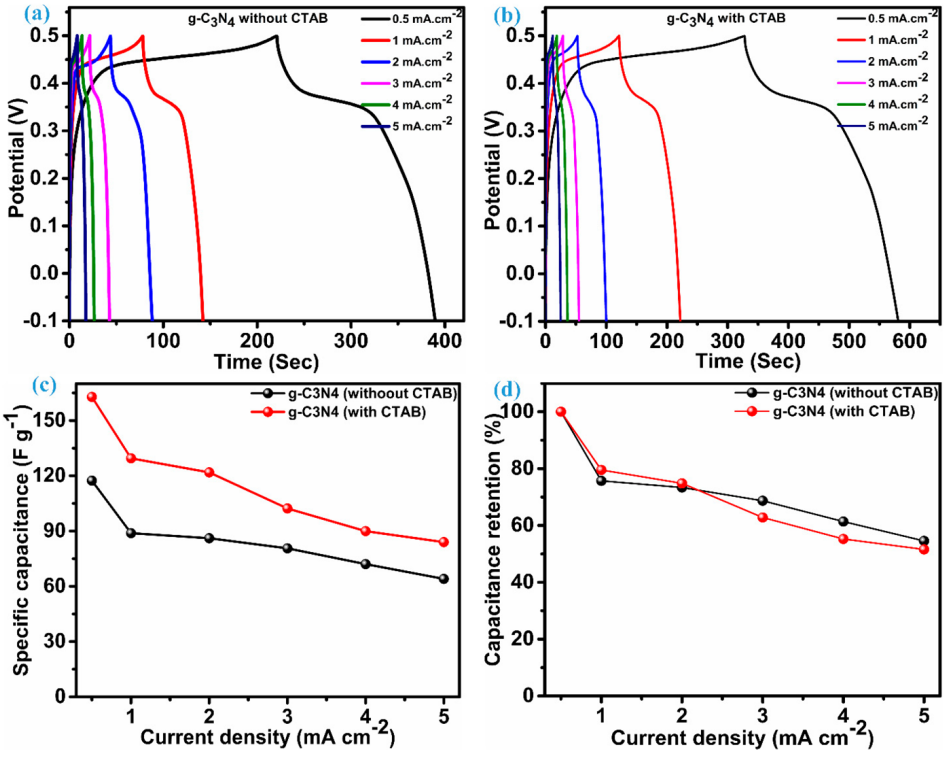

Figure 9. Electrochemical performance analysis, (**a**) GCD at different current densities of g-C_3N_4 without CTAB, (**b**) GCD at different current densities of g-C_3N_4 with CTAB, (**c**) specific capacitance at different current densities for both electrodes, (**d**) rate capability of both electrodes.

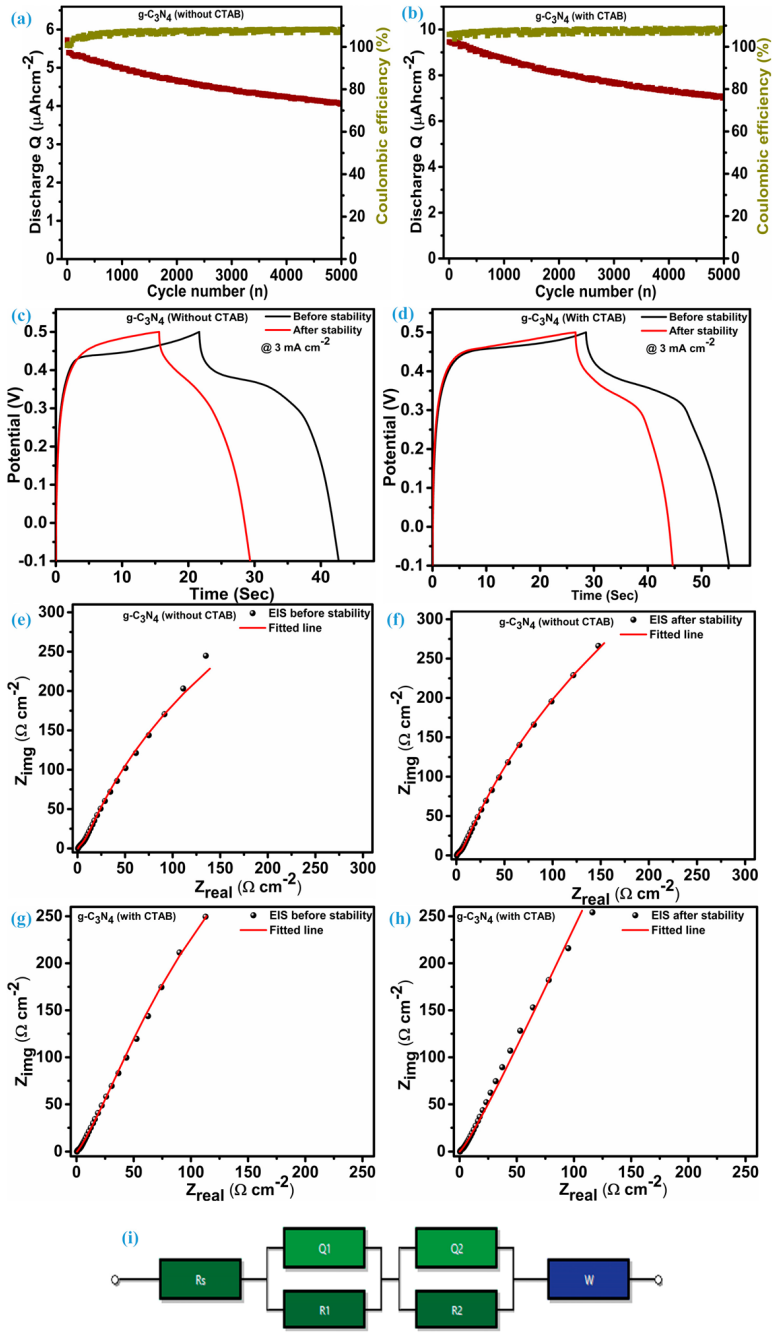

Figure 10. Stability and impedance analysis, (**a**) stability and coulombic efficiency of g-C_3N_4 without CTAB, (**b**) stability and coulombic efficiency of g-C_3N_4 with CTAB, (**c**) GCD before and after stability of g-C_3N_4 without CTAB at 3 mA cm^{-2}, (**d**) GCD before and after stability of g-C_3N_4 with CTAB at 3 mA cm^{-2}, (**e**,**f**) experimental and fitted EIS before and after stability of g-C_3N_4 without CTAB, (**g**,**h**) experimental and fitted EIS before and after stability of g-C_3N_4 with CTAB, and (**i**) equivalent circuit of fitting EIS.

4. Conclusions

In conclusion, the use of CTAB in crafting 2D graphitic carbon nitride (g-C_3N_4) sheets represents a significant leap in enhancing supercapacitive performance. The synergy between CTAB and g-C_3N_4 enhances structural characteristics, boosting surface area and conductivity for a more efficient charge storage mechanism. CTAB not only aids in forming well-defined 2D sheets but also preserves the structural integrity of g-C_3N_4 during synthesis. This advancement holds promise for practical applications in energy storage

devices, particularly high-performance supercapacitors crucial for portable electronics and renewable energy systems. In summary, the integration of CTAB in 2D g-C_3N_4 sheet preparation is a promising avenue for advancing supercapacitors.

Supplementary Materials: The following supporting information can be downloaded at: https://www.mdpi.com/article/10.3390/cryst14040312/s1, Figure S1: FE-SEM analysis after stability, (a–c) different magnification FE-SEM images of g-C3N4 without CTAB, and (d–f) different magnification FE-SEM images of g-C3N4 with CTAB; Figure S2: XPS analysis of CTAB integrated g-C3N4 on Ni-foam after stability (a) survey spectrum, (b) C 1s spectrum, and (c) N 1s spectrum; Table S1: Values of the elements connected in series estimated from the fitting of the EIS spectrum of the g-C3N4 samples before and after stability; Table S2: Comparative analysis of the electrochemical performance of g-C3N4-based electrodes.

Author Contributions: Conceptualization, S.M.M.; methodology, S.M.M.; software, S.M.M.; validation, A.M.T.; formal analysis, A.M.T. and S.A.B.; investigation, S.M.M. and D.R.P.; resources, S.A.B., D.R.P. and J.C.S.; data curation, D.R.P.; writing—original draft preparation, S.M.M.; writing—review and editing, S.M.M.; visualization, D.R.P., J.C.S. and J.L.; supervision, J.L.; project administration, J.L.; funding acquisition, J.L. All authors have read and agreed to the published version of the manuscript.

Funding: This research received no external funding.

Data Availability Statement: Dataset available on request from the authors.

Acknowledgments: This work was partly supported by the Korea Institute for Advancement of Technology (KIAT) grant funded by the Korean Government (Ministry of Trade, Industry, and Energy-MOTIE) (P0012770).

Conflicts of Interest: The authors declare no conflict of interest.

References

1. Ragupathi, V.; Panigrahi, P.; Ganapathi Subramaniam, N. g-C_3N_4 Doped MnS as High Performance Electrode Material for Supercapacitor Application. *Mater. Lett.* **2019**, *246*, 88–91. [CrossRef]
2. El-Sabban, H.A.; Attia, S.Y.; Diab, M.A.; Mohamed, S.G. Facile One-Pot Synthesis of Template-Free Porous Sulfur-Doped g-C_3N_4/Bi_2S_3 Nanocomposite as Efficient Supercapacitor Electrode Materials. *J. Energy Storage* **2023**, *60*, 106593. [CrossRef]
3. Sanati, S.; Rezvani, Z. g-C_3N_4 Nanosheet@CoAl-Layered Double Hydroxide Composites for Electrochemical Energy Storage in Supercapacitors. *Chem. Eng. J.* **2019**, *362*, 743–757. [CrossRef]
4. Maheshwaran, G.; Pandi, P.; Suganya, S.; Kumar, B.A.; Ramalingam, G.; Prabhu, M.R.; Sudhahar, S. Fabrication of Self Charging Supercapacitor Based on Two Dimensional Bismuthene-Graphitic Carbon Nitride Nanocomposite Powered by Dye Sensitized Solar Cells. *J. Energy Storage* **2022**, *56*, 105900. [CrossRef]
5. Chen, A.Y.; Zhang, T.T.; Qiu, Y.J.; Wang, D.; Wang, P.; Li, H.J.; Li, Y.; Yang, J.H.; Wang, X.Y.; Xie, X.F. Construction of Nanoporous Gold/g-C_3N_4 Heterostructure for Electrochemical Supercapacitor. *Electrochim. Acta* **2019**, *294*, 260–267. [CrossRef]
6. Rehman, J.; Eid, K.; Ali, R.; Fan, X.; Murtaza, G.; Faizan, M.; Laref, A.; Zheng, W.; Varma, R.S. Engineering of Transition Metal Sulfide Nanostructures as Efficient Electrodes for High-Performance Supercapacitors. *ACS Appl. Energy Mater.* **2022**, *5*, 6481–6498. [CrossRef]
7. Wang, X.; Fang, Y.; Shi, B.; Huang, F.; Rong, F.; Que, R. Three-Dimensional $NiCo_2O_4$@$NiCo_2O_4$ Core–Shell Nanocones Arrays for High-Performance Supercapacitors. *Chem. Eng. J.* **2018**, *344*, 311–319. [CrossRef]
8. Devarayapalli, K.C.; Lee, K.; Do, H.B.; Dang, N.N.; Yoo, K.; Shim, J.; Prabhakar Vattikuti, S.V. Mesostructured g-C_3N_4 Nanosheets Interconnected with V_2O_5 Nanobelts as Electrode for Coin-Cell-Type-Asymmetric Supercapacitor Device. *Mater. Today Energy* **2021**, *21*, 100699. [CrossRef]
9. Wang, X.; Shi, B.; Fang, Y.; Rong, F.; Huang, F.; Que, R.; Shao, M. High Capacitance and Rate Capability of a Ni_3S_2@CdS Core-Shell Nanostructure Supercapacitor. *J. Mater. Chem. A Mater.* **2017**, *5*, 7165–7172. [CrossRef]
10. Palchoudhury, S.; Ramasamy, K.; Gupta, R.K.; Gupta, A. Flexible Supercapacitors: A Materials Perspective. *Front. Mater.* **2019**, *5*, 83. [CrossRef]
11. Lokhande, P.E.; Chavan, U.S.; Bhosale, S.; Kalam, A.; Deokar, S. New-Generation Materials for Flexible Supercapacitors. In *Flexible Supercapacitor Nanoarchitectonics*; Wiley: Hoboken, NJ, USA, 2021; pp. 277–313. ISBN 9781119711469.
12. Yasami, S.; Mazinani, S.; Abdouss, M. Developed Composites Materials for Flexible Supercapacitors Electrode: "Recent Progress & Future Aspects". *J. Energy Storage* **2023**, *72*, 108807. [CrossRef]
13. Zhang, Y.; Li, X.; Wang, D.; Cai, J.; Chen, H.; Wei, D.; Yang, L.; Bai, L.; Liang, Y.; Yang, H. Lightweight Flexible Solid-State Supercapacitor Based on Graphene/Non-Woven Fabric Electrode. *Mater. Sci. Eng. B* **2023**, *294*, 116537. [CrossRef]
14. Rono, N.; Kibet, J.K.; Martincigh, B.S.; Nyamori, V.O. A Review of the Current Status of Graphitic Carbon Nitride. *Crit. Rev. Solid State Mater. Sci.* **2021**, *46*, 189–217. [CrossRef]

15. Balamuralitharan, B.; Cho, I.H.; Bak, J.S.; Kim, H.J. V_2O_5 Nanorod Electrode Material for Enhanced Electrochemical Properties by a Facile Hydrothermal Method for Supercapacitor Applications. *New J. Chem.* **2018**, *42*, 11862–11868. [CrossRef]
16. Vattikuti, S.V.P.; Reddy, B.P.; Byon, C.; Shim, J. Carbon/CuO Nanosphere-Anchored g-C_3N_4 Nanosheets as Ternary Electrode Material for Supercapacitors. *J. Solid. State Chem.* **2018**, *262*, 106–111. [CrossRef]
17. Duan, J.; Chen, S.; Jaroniec, M.; Qiao, S.Z. Porous C_3N_4 Nanolayers@n-Graphene Films as Catalyst Electrodes for Highly Efficient Hydrogen Evolution. *ACS Nano* **2015**, *9*, 931–940. [CrossRef] [PubMed]
18. Masar, M.; Urbanek, P.; Skoda, D.; Hanulikova, B.; Kozakova, Z.; Machovsky, M.; Munster, L.; Kuritka, I. Preparation and Characterization of Expanded g-C_3N_4 via Rapid Microwave-Assisted Synthesis. *Diam. Relat. Mater.* **2018**, *83*, 109–117. [CrossRef]
19. Zhang, G.; Lan, Z.A.; Wang, X. Surface Engineering of Graphitic Carbon Nitride Polymers with Cocatalysts for Photocatalytic Overall Water Splitting. *Chem. Sci.* **2017**, *8*, 5261–5274. [CrossRef]
20. Thomas, A.; Fischer, A.; Goettmann, F.; Antonietti, M.; Müller, J.O.; Schlögl, R.; Carlsson, J.M. Graphitic Carbon Nitride Materials: Variation of Structure and Morphology and Their Use as Metal-Free Catalysts. *J. Mater. Chem.* **2008**, *18*, 4893–4908. [CrossRef]
21. Dong, G.; Zhang, Y.; Pan, Q.; Qiu, J. A Fantastic Graphitic Carbon Nitride (g-C_3N_4) Material: Electronic Structure, Photocatalytic and Photoelectronic Properties. *J. Photochem. Photobiol. C Photochem. Rev.* **2014**, *20*, 33–50. [CrossRef]
22. Eid, K.; Gamal, A.; Abdullah, A.M. Graphitic carbon nitride-based nanostructures as emergent catalysts for carbon monoxide (CO) oxidation. *Green Chem.* **2023**, *25*, 1276–1310. [CrossRef]
23. Chen, L.; Maigbay, M.A.; Li, M.; Qiu, X. Synthesis and modification strategies of g-C_3N_4 nanosheets for photocatalytic applications. *Adv. Powder Mater.* **2024**, *3*, 100150. [CrossRef]
24. Tahir, M.; Cao, C.; Mahmood, N.; Butt, F.K.; Mahmood, A.; Idrees, F.; Hussain, S.; Tanveer, M.; Ali, Z.; Aslam, I. Multifunctional g-C_3N_4 Nanofibers: A Template-Free Fabrication and Enhanced Optical, Electrochemical, and Photocatalyst Properties. *ACS Appl. Mater. Interfaces* **2014**, *6*, 1258–1265. [CrossRef] [PubMed]
25. Zhang, J.; Ding, J.; Li, C.; Li, B.; Li, D.; Liu, Z.; Cai, Q.; Zhang, J.; Liu, Y. Fabrication of Novel Ternary Three-Dimensional RuO_2/Graphitic-C_3N_4@reduced Graphene Oxide Aerogel Composites for Supercapacitors. *ACS Sustain. Chem. Eng.* **2017**, *5*, 4982–4991. [CrossRef]
26. Gao, Y.; Zhao, W.; Zhang, D. Preparation of Prismatic g-C_3N_4 by CTAB Hydrothermal Method and Its Degradation Performance under Visible Light. *Diam. Relat. Mater.* **2022**, *121*, 108787. [CrossRef]
27. Ilager, D.; Shetti, N.P.; Reddy, K.R.; Tuwar, S.M.; Aminabhavi, T.M. Nanostructured Graphitic Carbon Nitride (g-C_3N_4)-CTAB Modified Electrode for the Highly Sensitive Detection of Amino-Triazole and Linuron Herbicides. *Environ. Res.* **2022**, *204*, 111856. [CrossRef] [PubMed]
28. Mane, S.M.; Wagh, K.S.; Teli, A.M.; Beknalkar, S.A.; Shin, J.C.; Lee, J. Mitigation of Shape Evolution and Supercapacitive Performance of $CuCo_2S_4$ Electrodes Prepared via a Simple Solvent Variation Approach. *Appl. Sci.* **2023**, *13*, 12122. [CrossRef]
29. Chen, P.; Xing, P.; Chen, Z.; Hu, X.; Lin, H.; Zhao, L.; He, Y. In-Situ Synthesis of $AgNbO_3$/g-C_3N_4 Photocatalyst via Microwave Heating Method for Efficiently Photocatalytic H_2 Generation. *J. Colloid. Interface Sci.* **2019**, *534*, 163–171. [CrossRef] [PubMed]
30. Qiao, F.; Wang, J.; Ai, S.; Li, L. As a New Peroxidase Mimetics: The Synthesis of Selenium Doped Graphitic Carbon Nitride Nanosheets and Applications on Colorimetric Detection of H_2O_2 and Xanthine. *Sens. Actuators B. Chem.* **2015**, *216*, 418–427. [CrossRef]
31. Fina, F.; Callear, S.K.; Carins, G.M.; Irvine, J.T.S. Structural Investigation of Graphitic Carbon Nitride via XRD and Neutron Diffraction. *Chem. Mater.* **2015**, *27*, 2612–2618. [CrossRef]
32. Antil, B.; Kumar, L.; Ranjan, R.; Shenoy, S.; Tarafder, K.; Gopinath, C.S.; Deka, S. One-Dimensional Multichannel g-$C_3N_{4.7}$Nanostructure Realizing an Efficient Photocatalytic Hydrogen Evolution Reaction and Its Theoretical Investigations. *ACS Appl. Energy Mater.* **2021**, *4*, 3118–3129. [CrossRef]
33. Li, J.; Wang, Y.; Wang, Y.; Guo, Y.; Zhang, S.; Song, H.; Li, X.; Gao, Q.; Shang, W.; Hu, S.; et al. MXene Ti_3C_2 decorated g-C_3N_4/ZnO photocatalysts with improved photocatalytic performance for CO_2 reduction. *Nano Mater. Sci.* **2023**, *5*, 237–245. [CrossRef]
34. Mo, Z.; She, X.; Li, Y.; Liu, L.; Huang, L.; Chen, Z.; Zhang, Q.; Xu, H.; Li, H. Synthesis of g-C_3N_4 at different temperatures for superior visible/UV photocatalytic performance and photoelectrochemical sensing of MB solution. *RSC Adv.* **2015**, *5*, 101552–101562. [CrossRef]
35. Su, D.S.; Zhang, J.; Frank, B.; Thomas, A.; Wang, X.; Paraknowitsch, J.; Schlögl, R. Metal-Free Heterogeneous Catalysis for Sustainable Chemistry. *ChemSusChem* **2010**, *3*, 169–180. [CrossRef] [PubMed]
36. Zhou, A.Q.; Yang, J.M.; Zhu, X.W.; Zhu, X.L.; Liu, J.Y.; Zhong, K.; Chen, H.X.; Chu, J.Y.; Du, Y.S.; Song, Y.H.; et al. Self-assembly construction of NiCo LDH/ultrathin g-C_3N_4 nanosheets photocatalyst for enhanced CO_2 reduction and charge separation mechanism study. *Rare Met.* **2022**, *41*, 2118–2128. [CrossRef]
37. Vinu, A. Two-Dimensional Hexagonally-Ordered Mesoporous Carbon Nitrides with Tunable Pore Diameter, Surface Area and Nitrogen Content. *Adv. Funct. Mater.* **2008**, *18*, 816–827. [CrossRef]
38. Wellia, D.V.; Syafawi, A.; Putri, Y.E.; Muldarisnur. The effect of cetyltrimethylammonium bromide (CTAB) addition on green synthesis of porous N-doped TiO_2 for photoreduction of heavy metal ion Cr(VI). *RSC Adv.* **2023**, *13*, 29645–29656. [CrossRef] [PubMed]
39. Balamurugan, J.; Li, C.; Aravindan, V.; Kim, N.H.; Lee, J.H. Hierarchical Ni-Mo-S and Ni-Fe-S Nanosheets with Ultrahigh Energy Density for Flexible All Solid-State Supercapacitors. *Adv. Funct. Mater.* **2018**, *28*, 1803287. [CrossRef]

40. Zhang, X.; Liao, H.; Liu, X.; Shang, S.; Zhou, Y.; Zhou, Y. Graphitic carbon nitride nanosheets made by different methods as electrode material for supercapacitors. *Ionics* **2020**, *26*, 3599–3607. [CrossRef]
41. Mariappan, V.K.; Krishnamoorthy, K.; Pazhamalai, P.; Natarajan, S.; Sahoo, S.; Nardekar, S.S.; Kim, S.J. Antimonene Dendritic Nanostructures: Dual-Functional Material for High-Performance Energy Storage and Harvesting Devices. *Nano Energy* **2020**, *77*, 105248. [CrossRef]
42. Mohamed, S.G.; Hussain, I.; Shim, J.J. One-Step Synthesis of Hollow C-$NiCo_2S_4$ Nanostructures for High-Performance Supercapacitor Electrodes. *Nanoscale* **2018**, *10*, 6620–6628. [CrossRef]
43. Chowdhury, A.; Biswas, S.; Sharma, V.; Halder, J.; Dhar, A.; Sundaram, B.; Dubey, B.; Burada, P.S.; Chandra, A. High Performance Magnetic Pseudocapacitors—Direct Correlation between Specific Capacitance and Diffusion Coefficients. *Electrochim. Acta* **2021**, *397*, 139252. [CrossRef]
44. Kirubasankar, B.; Narayanasamy, M.; Yang, J.; Han, M.; Zhu, W.; Su, Y.; Angaiah, S.; Yan, C. Construction of Heterogeneous 2D Layered MoS_2/MXene Nanohybrid Anode Material via Interstratification Process and Its Synergetic Effect for Asymmetric Supercapacitors. *Appl. Surf. Sci.* **2020**, *534*, 147644. [CrossRef]
45. Huang, H.; Cui, J.; Liu, G.; Bi, R.; Zhang, L. Carbon-Coated $MoSe_2$/MXene Hybrid Nanosheets for Superior Potassium Storage. *ACS Nano* **2019**, *13*, 3448–3456. [CrossRef] [PubMed]
46. Isacfranklin, M.; Yuvakkumar, R.; Ravi, G.; Velauthapillai, D.; Pannipara, M.; Al-Sehemi, A.G. Superior Supercapacitive Performance of Cu_2MnSnS_4 asymmetric Devices. *Nanoscale Adv.* **2021**, *3*, 486–498. [CrossRef]